# Characterization of the role of spatial proximity of DNA double-strand breaks in the formation of CRISPR-Cas9-induced large structural variations

Mikkel Dahl-Jessen*[1,2], Thorkild Terkelsen*[#1,2,3], Rasmus O. Bak[1,4], and Uffe Birk Jensen[#2,3,]

1. Department of Biomedicine, Aarhus University, Aarhus, Denmark

2. Department of Clinical Medicine, Aarhus University, Aarhus, Denmark

3. Department for Clinical Genetics, Aarhus University Hospital, Aarhus, Denmark

4. Aarhus Institute of Advanced Studies (AIAS), Aarhus University, Aarhus, Denmark

* These authors contributed equally to the manuscript.

# Corresponding authors: Thorkild Terkelsen (thorkild.terkelsen@biomed.au.dk) and Uffe Birk Jensen (uffejens@rm.dk)

## Abstract

Structural variations (SVs) play important roles in genetic diversity, evolution, and carcinogenesis and are, as such, important for human health. However, it remains unclear how spatial proximity of double-strand breaks (DSBs) affects the formation of SVs. To investigate if spatial proximity between two DSBs affects DNA repair, we used data from 3C experiments (Hi-C, ChIA-PET, and ChIP-seq) to identify highly interacting loci on six different chromosomes. The target regions correlate with the borders of mega-base sized Topologically Associated Domains (TADs), and we used CRISPR-Cas9 nuclease and pairs of single guide RNAs (sgRNAs) against these targets to generate DSBs in both K562 cells and H9 human embryonic stem cells (hESC). Droplet Digital PCR (ddPCR) was used to quantify the resulting recombination events, and high-throughput sequencing was used to analyze the chimeric junctions created between the two DSBs.

We observe a significantly higher formation frequency of deletions and inversions with DSBs in proximity as compared to deletions and inversions with DSBs not in proximity in K562 cells. Additionally, our results suggest that DSB proximity may affect the ligation of chimeric deletion junctions. Taken together, spatial proximity between DSBs is a significant predictor of large-scale deletion and inversion frequency induced by CRISPR-Cas9 in K562 cells. This finding has implications for understanding SVs in the human genome and for the future application of CRISPR-Cas9 in gene editing and the modelling of rare SVs.

## Introduction

Structural variants (SVs) encompass a variety of DNA alterations, including inversions, deletions, and insertions of DNA segments. While many SVs are without clinical significance, some SVs that arise in germ cells lead to genetic disorders, and some that arise in somatic cells contribute to the development of cancer (Yoshioka et al. 2021). SVs can be created by CRISPR-Cas9 genome editing via two double-strand breaks (DSBs) that occur at the target sites of two different sgRNAs, which we refer to as an sgRNA pair, or at multiple target sites of an individual sgRNA (Cullot et al. 2019; Höijer et al. 2022; Wu et al. 2022) Unequal crossing over is a common and well described mechanism for the creation of duplications and deletions. However, SV formation could also be influenced by other factors such as the three-dimensional genomic structure, as breakpoint proximity has been associated with both recurrent translocation formation (Nikiforova et al. 2000), and non-recurrent translocation formation (Rothkamm et al. 2001; Engreitz et al. 2012; Zhang et al. 2012; Balajee et al. 2018; Eidelman et al. 2021). Furthermore, SV breakpoints have been shown to correlate with interaction frequencies measured by Hi-C (Gandhi et al. 2006; Swenson and Blanchette 2019; Akdemir et al. 2020; Sidiropoulos et al. 2022). These findings support that DSB proximity may play a role in SV formation, although this understanding has not been verified with genome engineering in a controlled manner. DNA has also shown the ability to shift position in the three-dimensional nucleus upon induction of DSBs in a process called “DSB clustering” (Aten et al. 2004; Roukos et al. 2013; Aymard et al. 2017; Arnould et al. 2023). Thus, two opposing understandings of SV formation have emerged, the “contact first” vs “breakage first” model (Misteli and Soutoglou 2009).

The development of Hi-C and Hi-C-related techniques in recent years have led to the discovery of Topologically Associated Domains (TADs), which are loop-like genomic structures characterized by extensive self-interaction. TADs are established through a dynamic interplay between CTCF and cohesin, influenced by the orientation of the CTCF motif. Accumulation of CTCF and cohesin occurs at specific sites, known as TAD borders (Fudenberg et al. 2016). TAD borders are excellent candidates to verify spatial proximity effects experimentally, as they exhibit consistent interaction across the cell cycle and cell types (Fudenberg et al. 2016; Schmitt et al. 2016; Krefting et al. 2018), and because advances in Hi-C and related techniques offer high-resolution TAD border capture (Lieberman-Aiden et al. 2009; Dixon et al. 2012).

SVs are generally formed through non-allelic homologous recombination, replicative mechanisms, or canonical non-homologous end joining (c-NHEJ) (Gu et al. 2008; Liu et al. 2012). In studies with irradiation-induced DSBs, c-NHEJ has been shown to repair DNA with biphasic kinetics involving a fast and a slow process depending on chromatin context (DiBiase et al. 2000; Riballo et al. 2004; Biehs et al. 2017). The fast

c-NHEJ process occurs in the G1 and G2 phases of the cell cycle and is resection-independent (Biehs et al. 2017). The slow c-NHEJ process occurs in the G1 phase. This process is resection-dependent and requires the endonuclease Artemis. The slow process is characterized by microhomology usage and is more error-prone than fast c-NHEJ. It is primarily associated with repairing DSBs in heterochromatin (Biehs et al. 2017). Yet, it is unknown if DSB proximity could change SV formation kinetics and junction characteristics in a similar manner.

In this study, we quantify the impact of spatial proximity on SV formation by targeting borders of highly conserved TADs with DSBs induced by CRISPR-Cas9, comparing the results to size-matched non-interacting loci. Additionally, we investigate whether proximity between DSBs induced by CRISPR-Cas9 affects SV formation kinetics and repair characteristics of chimeric deletion junctions.

## Results

### Spatial proximity between DSBs increases SV formation in K562 cells

To investigate the impact of spatial proximity on CRISPR-Cas9 induced SV formation, we first identified six distinct TADs using publicly available HiC and ChIA-PET data (Fig 1A and 1B). We also used ChIP-seq data for cohesin, RAD21, SMC3, and CTCF, including motif orientation, to show enrichment and conservation of TAD border markers (Supplemental Figs S1-S6). We then designed sgRNAs to target the six TADs at seven to eight distinct positions (sgRNAs A-H, see Methods). By combining these in pairs, the sgRNA pairs would induce DSBs in spatial proximity inside (AB) and outside (CD) the CTCF motifs at TAD borders, at spatially distant positions (EF) or at non-related TAD borders (GX). The sgRNAs were designed to generate DSBs at a similar linear distance from each other (Fig 1A and 1B). The frequency of SVs formed between the two DSBs was quantified by ddPCR assays designed to detect both deletions and inversions (Fig 1C).

We hypothesized that a significant difference in SV frequency (defined as the sum of deletion and inversion frequencies) between sgRNA pairs AB and CD at TAD borders could result from steric hindrance of Cas9 caused by cohesin occupying the borders. Furthermore, we hypothesized that any difference between sgRNA pairs EF and GX would be due to DSB vulnerability at TAD borders (Canela et al. 2017a). Therefore, we compared SV frequencies in sgRNA pairs AB with CD and EF with GX. There was no significant difference between AB (median 30%) and CD (median 27%) and thus no effect of the position relative to the binding site of CTCF/cohesin on SV frequency ($p = 0.94$) (Fig 1D). Similarly, there was no significant difference between EF (median 13%) and GX (median 22%), and thus no significant effect from TAD DSB vulnerability

with the caveat of a limited sample size (p = 0.24) (Fig 1D). Thus, we grouped sgRNA pairs AB and CD as "proximity" and EF and GX as "non-proximity", although we could not exclude that the pooled groups could differ according to additional factors that could influence the results despite no statistically significant difference in SV frequency.

Spatial proximity was associated with a significant increase in the formation of SVs, which increased from a median frequency of 18% in the non-proximity group to a median frequency of 30% in the proximity group (p = 0.004) (Fig 1E). Because the formation of SVs could be influenced by the cutting efficiencies of the individual sgRNAs in the pairs, we performed Sanger sequencing across all cut sites and estimated the frequency of indels less than 30bp as an indicator of sgRNA efficiency using the Inference of CRISPR Edits (ICE) tool. The individual sgRNA efficiencies, measured by their ability to facilitate indels at their target sites, also correlated with the frequency of SVs (Spearman r = 0.45, p = 0.03) (Supplemental Fig S11), but the sgRNA efficiencies did not differ significantly between the proximity and non-proximity groups (Fig 1F).

The increase in SV frequency between proximity and non-proximity groups corresponded to a significant increase in deletion frequency (p = 0.002), but not significantly in inversion frequency (p = 0.06) (Supplemental Fig S12A). We did not observe a significant difference when comparing the frequency of deletions and inversions (p = 0.07) (Fig 1G). As shown later, resection of DNA may occur at the chimeric deletion junctions between the two DSBs due to imprecise ligation. Such DNA resections could lead to disruption of ddPCR primers and/or probes, but high-throughput sequencing of the chimeric junctions revealed no significant difference in ddPCR detectable deletions between the proximity and non-proximity groups (p = 0.53) (Supplemental Fig S10C). Thus, the observed association between proximity and SV frequency was not influenced by differences in ddPCR sensitivity.

**Effect of DSB proximity in human embryonic stem cells**

Having observed that spatial proximity affected the formation of CRISPR-Cas9-induced SVs in K562 cells, we subsequently investigated if spatial proximity also affected the formation of SVs in non-cancer cells. Hence, we repeated the previous experiment for H9 human embryonic stem cells (hESCs) using the same sgRNA pairs, albeit without the Chr10 TAD locus. Similar to K562 cells, we confirmed that neither cohesin nor TAD borders affected our results (see Fig 2A). Hence, as previously, we grouped sgRNA pairs AB and CD as "proximity", and sgRNA pairs EF and GX as "non-proximity".

The median frequency of SVs in H9 hESCs was 1.8% in the non-proximity group and 3.8% in the proximity group, which was not statistically significantly different (p = 0.14) (Fig 3C). Any increase in SV frequency was also not statistically significant for deletion (p = 0.17) or inversion frequency (p = 0.12) (Supplemental Fig S12B). As for K562 cells, we did not observe a difference between the frequencies of deletions and inversions in H9 hESCs (p = 0.10) (Fig 2C). Altogether, we could not confirm that DSB spatial proximity was associated with an increase in the formation of SVs in human embryonic stem cells with the caveat that the SV frequencies were an order of magnitude lower in H9 hESCs than in K562 cells.

We also assessed the capability of individual sgRNAs to induce indels at their target sites in H9 hESCs. In an analysis of indel frequencies at the sgRNA cut sites using the ICE tool, which has a reported lower sensitivity of 5% indel frequency, 32 out of 35 sgRNAs did not generate detectable indel frequencies, yet still facilitated the formation of SVs. Indel frequency at the cut sites of the sgRNAs measured by Sanger sequencing could thus be an unreliable indicator of sgRNA efficiency in H9 hESCs due to the limited sensitivity of this analysis (Fig 2D).

Notably, the CRISPR-Cas9 targets in the proximity group had significantly lower HiC scores in hESCs compared to in K562 cells (p = 0.004) (Supplemental Fig S13), possibly suggesting that the target TADs were less conserved in hESC than in K562 cells.

**Effect of DSB proximity on SV formation speed**

Having observed that spatial proximity of DSBs affected the formation frequency of SVs in K562 cells, we hypothesized that the distance between the DSBs might also affect the speed of SV formation.

To investigate the speed of SV formation, we compared the cumulative frequency of SVs at various time points to the endpoint frequency. This experiment did not confirm that formation of SVs occurred earlier in the proximity group compared to the non-proximity group. For example, at 12 hours after electroporation the median cumulative frequency of deletion formation was 51% in the proximity group and 31% in the non-proximity group, which was not statistically significantly different (p = 0.06) (Fig 3A and 3B). By comparison, inversion formation 12 hours after electroporation was 54% in the proximity group and 36% in the non-proximity group showing a statistically significant difference (p = 0.03) (Fig 3C and 3D). However, we noted that the kinetic profile of our GX sgRNA pairs resembled that of the proximity group rather than that of the sgRNA pairs EF (Fig 3A and 3C).We did not observe any difference in the speed of formation between deletions and inversions (Fig 3E).

**Effect of DSB proximity on ligation of SV junctions**

We hypothesized that utilization of fast c-NHEJ for SV formation would require proximity between DSBs. To assess this, we employed high-throughput amplicon sequencing on five chimeric deletion junctions for each of the sgRNA pairs AB, CD, EF and GX. We centered our analysis on resection-independent end joining and microhomology usage, as these are readily measurable metrics that are characteristic of either fast or slow c-NHEJ (Biehs et al. 2017). A chimeric deletion junction was defined as the ligation product of a deletion made with one of the sgRNA pairs (Fig 4A). Resection-independent endjoining was measured in terms of precise ligation of the chimeric deletion junctions. Here, we defined precise ligation as a chimeric deletion junction with up to two bp insertions to account for templated insertions (Guo et al. 2018) and up to two bp resections to account for staggered cuts being generated by Cas9 (Xue and Greene 2021). Thus, chimeric deletion junctions could be ligated in four ways: 1) precise ligation(Guo et al. 2018)(Xue and Greene 2021), 2) insertions >2 bp, 3) resections >2 bp, and 4) mixed resections and insertions >2 bp (Fig 4B). The distribution of ligation outcomes in the proximity group and in the non-proximity group is illustrated (Fig 4C).

The proximity group showed a significant increase in precise ligation of chimeric deletion junctions to 58.86 % compared to 41.63 % in the non-proximity group ($p = 0.04$), which suggested increased usage of the resection-independent fast c-NHEJ process (Fig 4D). As a sensitivity analysis, we tested whether excluding 1-2 bp resections from the definition of precise ligation would significantly affect the results. Precise ligation differences were not significant with this definition ($p = 0.089$) (Supplemental Fig S14A). There was no significant difference between precise ligation of the GX sgRNA pairs and the EF sgRNA pairs, which suggested no significant influence from TAD border nucleotide homology ($p = 0.222$) (Supplemental Fig S14B).

Finally, the proximity group showed a signification reduction in microhomology-usage at resected junctions compared to the non-proximity group ($p = 0.04$) (Fig 4E). Taken together, the increase in precise ligation and the reduction in microhomology-usage in the proximity group compared to the non-proximity group could suggest a difference in DSB repair with increased usage of the fast c-NHEJ pathway compared to the slow c-NHEJ pathway. However, the observed differences were only borderline significant, so we did not interpret the evidence to be conclusive.

## Discussion

In this study, we investigated experimentally if spatial proximity between CRISPR-Cas9-generated DSBs would affect the frequency of deletion and inversion formation. The idea that spatial proximity of DSBs would affect the formation of SVs is not new, however, as multiple lines of prior evidence had established a connection between breakpoint proximity and SVs. Thus, FISH analysis was used to demonstrate that a known recurrent translocation occurred between loci in spatial proximity (Nikiforova et al. 2000). Another study observed that low dose irradiation yielded fewer non-recurrent SVs than high-dose irradiation, which the authors suggested could be due to more spatiotemporal separation of DSBs in the low dose group (Rothkamm et al. 2001). The development of HiC since then allowed the validation of these findings, revealing that non-recurrent translocations induced by irradiation often involve loci with increased HiC interaction (Engreitz et al. 2012; Zhang et al. 2012; Balajee et al. 2018; Eidelman et al. 2021). Moreover, computational modelling linked non-translocation SV breakpoints with increased HiC interaction (Swenson and Blanchette 2019). While these studies showed a correlation between spatial proximity and both recurrent and non-recurrent SV formation, they did not establish causality or quantified the impact of spatial proximity. In this study, we verify using genome engineering that spatial proximity between DSBs significantly increases SV frequency in K562 cells (Fig 1E). Although we did not reach statistical significance when replicating the experiment in another cell line, H9 hESC (Fig 2B), it is possible that the observed effect in K562 cells also applies to other cell lines, as the replicate analysis was underpowered and limited by significantly lower HiC interaction strength between sgRNA pairs in the proximity group compared to K562 cells (Supplemental Fig S13).

Our results align with the previous studies, reinforcing the idea that spatial proximity between DSBs has a significance in the generation of SVs. This idea, often referred to as the “contact first” hypothesis of SV formation, has been challenged by numerous studies showing that DSB loci cluster in space (Aten et al. 2004; Roukos et al. 2013; Aymard et al. 2017; Arnould et al. 2023), which has led to a contrasting “breakage first” hypothesis of SV formation (Misteli and Soutoglou 2009). Although we did not investigate DSB clustering specifically, we consider our work a relevant contribution to the debate.

Through the use of CRISPR-Cas9 in the generation of SVs, we also show that spatial proximity could be a relevant parameter to consider for CRISPR-Cas9 gene editing strategies, particularly those involving large DNA excisions using CRISPR-Cas9 pairs. A well-described example is the creation of microdystrophin through truncation of the DMD gene in Duchenne's Muscular Dystrophy (Min et al. 2019). Additionally, DSB proximity could serve as a valuable parameter to consider, when assessing the feasibility of modelling large

SVs within a cell line with CRISPR-Cas9 pairs. This approach is otherwise often restricted by low efficiency (Choi and Meyerson 2014).

The notable variability in our data, however, implies that spatial proximity should not be regarded as an absolute predictor of increased SV formation. Rather, it could be considered as one of several parameters, such as transcriptional activity, cell type, chromatin state and cell cycle (Canoy et al. 2022). Specifically for CRISPR-Cas9 induced SVs, sgRNA efficiency is a known predictor of SV frequency (Choi and Meyerson 2014). In our study, the ability of an sgRNA to generate indels was also independently associated with higher SV frequency in K562 (Supplemental Fig S11), but not in H9 hESC, where most sgRNAs did not produce indels despite being capable of creating SVs (Supplemental Table S8). Similar to a recent finding in human primary cells (Selvaraj et al. 2024), we therefore caution that indel frequency might not reflect actual DSB frequency in all cell lines. A recent study showed that individual sgRNA efficiency could be affected by the number of spatial interactions at its DNA target (Bergman and Tuller 2024). Similar to our finding, this underlines the importance of evaluating 3D genomic context for CRISPR-Cas9 experiments.
Regarding the generation of large CRISPR-Cas9-induced SVs, it is also notable that deletion and inversion frequencies were similar in our experiments (Fig 1G, Fig 2C). This observation aligns with a prior study that generated a 2.5 mb deletion using an sgRNA pair (Miyata et al. 2023). However, it differs from another study that suggested a preference for deletions over inversions when inducing small SVs with sgRNA pairs (Watry et al. 2020).

We also investigated if spatial proximity impacted the underlying repair dynamics of SV formation, hypothesizing that utilization of fast c-NHEJ for SV formation would require proximity between DSBs. Our hypothesis was based on the knowledge that fast and slow c-NHEJ both share a similar first step in their repair pathways (Biehs et al. 2017). This step involves the rapid recruitment of the Ku70/80 protein to DSBs, which, in turn, facilitates the recruitment of additional repair factors, such as DNA-PKcs. Together, these repair factors form a synapsis between DNA ends that guards against the formation of SVs (Frit et al. 2019; Watanabe and Lieber 2023).

Although we observed that deletions from proximity DSBs showed more precise ligation (Fig 4D) and less microhomology-usage (Fig 4E) compared to deletions from non-proximity DSBs, which are characteristics associated with the fast c-NHEJ repair pathway (Biehs et al. 2017), we did not detect a statistically significant difference in SV formation speed, except at a single time point for inversions (Fig 3D). Furthermore, the sgRNA pairs, which targeted non-proximity TAD borders, GX, had a kinetics and precise

ligation profile similar to the proximity sgRNA pairs rather than the other non-proximity sgRNA pairs targeting inter-TAD loci (Fig 3A, Fig 3C, Supplemental Fig S14B). Thus, the kinetics and precise ligation differences could be explained by other factors than proximity. Also, precise ligation differences were not significant in a sensitivity analysis with an alternate definition of precise ligation (Supplemental Fig S14A). More research is therefore warranted to investigate if proximity changes DSB repair dynamics.

Nonetheless, it is interesting how SVs arise, when DSBs are not in proximity, as Ku-PKcs synapses are expected to keep the original free DNA ends together. However, studies have demonstrated that these synapses can break when Ku70/80 or DNA-PKcs are phosphorylated (Uematsu et al. 2007; Lee et al. 2016), potentially allowing for DNA movement through space and the subsequent formation of SVs through slow c-NHEJ. SVs without DSB proximity could also emerge in a Ku-PKcs independent manner, a process referred to as alternative-NHEJ (alt-NHEJ) (Chang et al. 2017), although this is less likely, as human cells do not typically utilize alt-NHEJ when Ku is present, neither when repairing DSBs induced by irradiation (Biehs et al. 2017) or DSBs induced by designer nucleases (Ghezraoui et al. 2014).

Our study had some notable limitations. Firstly, many parameters are likely to influence SV frequency as previously discussed. Thus, comparing SV frequency at different loci is an inherent limitation of our study design. Secondly, we assumed conservation of TAD borders across different cell lines (Schmitt et al. 2016; Krefting et al. 2018), as this allowed us to reuse the same sgRNAs for hESC as for K562 cells. However, when we analyzed HiC interaction between the breakpoints in the proximity group in both hESC and K562 cells, the interaction was significantly lower in hESC, indicating less TAD conservation in hESC than K562 cells (Supplemental Fig S13). We also observed slight length variations in CTCF ChIA-PET interactions for each of the targeted TADs (Supplemental Fig S1-6). Since HiC and ChIA-PET data only represent the statistically most predominant average configurations within the cell population (Chang et al. 2020), this suggests that there were subtle differences in TAD extent within the K562 cell population. A recent review also challenged the notion of TAD conservation (Eres and Gilad 2021). Our assumption of TAD border conservation could therefore have led to a slight underestimation of the impact of spatial proximity.

Thirdly, the quantification of SV frequency from sgRNA pairs targeting non-related TAD borders, GX, was not part of the original study design and DNA was thus not extracted simultaneously with AB, CD and EF for each TAD locus in K562 cells. Thus, it is important to note that inter-experimental variation could have affected our results despite the high transfection efficiencies we usually obtain in experiments with this immortal, fast-growing cell line. Moreover, we noticed that the sgRNA pairs GX appeared to have higher SV

frequencies compared to the sgRNA pairs EF targeting inter-TAD loci (Fig 1D, Fig 2A). Although differences were not statistically significant, TAD borders are known to accumulate torsion from transcription induced negative supercoiling of DNA (Racko et al. 2018), which can cause DSBs (Canela et al. 2017a) and drive SV formation (Wu et al. 2017; Krefting et al. 2018). Potentially, this intrinsic propensity could have contributed to an overestimation of the true effect of spatial proximity in our study. Precise ligation at chimeric deletion junctions also seemed more prevalent for these sgRNA pairs compared to sgRNA pairs targeting inter-TAD loci (Supplemental Fig S14B), indicating that nucleotide homology between TAD borders could have influenced the precise ligation analysis.

Fourthly, we decided to categorize 1-2 bp indels at chimeric deletion junctions as precise ligation to account for CRISPR-Cas9-induced staggered ends (Xue and Greene 2021), yet a study of induced SVs in *Arabidopsis* did not (Beying et al. 2020). Such classification differences make comparisons difficult and accentuates the need for a standardized approach.

Lastly, we did not adjust for multiple testing in this study. The CRISPR-Cas9 experiments were specifically designed to test the hypothesis that spatial proximity between DSBs might affect the frequency of CRISPR-Cas9-induced SVs, which meant that multiple testing was unlikely to affect the main conclusions. However, as our observations prompted us to initiate additional investigations to explore e.g. differential DSB repair mechanisms, we cannot exclude that some of the borderline statistically significant differences could be affected by chance, which underlines the need for future studies to explore this area.

Although our work offers evidence suggesting that DSB proximity increases SV frequency, the limitations of our study highlight the need for further experimental validation to definitively determine if and how DSB proximity influences SV formation.

# Methods

### Experimental design

To investigate the impact of spatial proximity on CRISPR-Cas9 induced SV formation (defined as deletions or inversions occurring between two DSBs), single guide RNAs (sgRNAs) were designed for TADs on the Chromosomes (Chr) 2, 6, 10, 17, 21 and X. At each TAD locus, sgRNA targets were identified at the four edges surrounding the interacting TAD borders (targets A, B, C and D), at two non-interacting sites distant from the TAD borders (targets E and F) and at a CTCF-binding region that did not spatially interact with the borders of the studied TAD (targets G and H). The sgRNAs were paired for targets A and B (sgRNA pairs AB)

at the proximal edges, i.e. inside, of the TAD borders, for targets C and D (CD) at the distal edges, i.e. outside, of the TAD borders, for targets E and F (EF) away from the TAD borders, and for targets G and either A, B or H (GX) at non-related (i.e., non-mutually interacting) TAD borders. The G and H targets were designed in a later phase of the study, due to reports that TAD borders could be more vulnerable to DSBs than non-TAD loci (Canela et al. 2017b), and therefore not included in the initial experiments. The targets were designed such that the linear distance in nucleotides between the sgRNAs in each pair should be approximately the same for all sgRNA pairs at each TAD. To adhere to this rule, the additional target H was designed for Chr10 because none of the sgRNAs A, B, C or D could be paired with G to keep the linear distance approximately the same for GX as for the other sgRNA pairs. The sgRNA pairs were tested one pair by one with no multiplexing of the sgRNA pairs in transfections to prevent unwanted interference between multiple cut sites.

The primary aim of the study was to measure the frequency of large deletions and inversions generated by CRISPR-Cas9 depending on spatial proximity of the DSBs. A secondary aim was to explore for temporal trends in the development of these SVs. Thus, CRISPR-Cas9 experiments were performed in human myeloid K562 cells with the sgRNA pairs AB, CD, EF and GX for all six TADs (Chr2, Chr6, Chr10, Chr17, Chr21 and ChrX) and analysed for deletions and inversions at several time points (3, 6, 12, 24 and 48-72 hours). For feasibility, this time course experiment was divided over multiple experimental sessions, one TAD at a time, so that AB, CD and EF were repeated in the same session. The later designed sgRNA pair GX was investigated for all TADs and time points in a single experimental session separate in time from the other sgRNA pairs. Additionally, the time course experiment was repeated in a later session for the sgRNA pair EF on Chr10 after re-synthesis of the non-functional sgRNA E for Chr10, which had failed in the original experiments due to production error. Thus, the experiment was divided over a total of 8 sessions of transfections (n = 6 sessions for AB, CD and EF, one TAD at a time; n = 1 session for GX, all TADs; 1 session for repeating EF, only the Chr10 TAD).

For biological replication, CRISPR-Cas9 was repeated in H9 human embryonic stem cells (hESC) in a replication experiment that included all four sgRNA pairs (AB, CD, EF and GX) for five of the six TADs (Chr2, Chr6, Chr17, Chr21 and ChrX) with DNA extraction at a single time point (72 hours) during the same experimental session. The TAD on Chr10 was not included in the H9-ESC experiment due to failure of sgRNAs to generate indels in K562 cells. In addition to these primary analyses, high-throughput sequencing of the deletion junctions in K562 cells was performed to explore the sequence composition of the ligated junctions.

**Locating TAD borders in the human genome with high resolution**

TAD borders are discernible as clustered inter-ligation Paired-End Tags (PETs) in Chromatin Interaction Analysis by Paired-End Tag sequencing (ChIA-PET) for CTCF (Tang et al. 2015) and as corner-dots in HiC heat maps (Lieberman-Aiden et al. 2009; Beagan and Phillips-Cremins 2020). Furthermore, they are characterized by accumulation of CTCF and cohesin, which can be identified by Chromatin Immunoprecipitation sequencing (ChIP-seq). These idiosyncratic features of TAD borders allow for their precise identification using HiC, ChIA-PET, and ChIP-seq data (Sadowski et al. 2019).

To locate TAD borders for CRISPR-Cas9 targeting, publicly available ChIA-PET data for CTCF in K562 cells (Tang et al. 2015) (ENCODE: ENCFF000KYD) were therefore stratified for size and confidence score and the six largest, most confident inter-ligation PETs (avg. size 1.85 megabases [range: 0.9-3 megabases]) were selected. The inter-ligation PETs were then visualized in the UCSC Genome Browser and compared with K562 HiC data (Rao et al. 2014) to assess whether the PETs corresponded with TAD border characteristic corner-dots in heat maps (Beagan and Phillips-Cremins 2020). Furthermore, enrichment of evolutionary conserved CTCF and cohesin (RAD21 and SMC3) traces were confirmed using publicly available ChIP-seq data (Davis et al. 2018) (Supplemental Table S1) and CTCF motif orientation assessed using the JASPAR database (Supplemental Fig S1-S6). In case of a TAD comprising multiple inter-ligation PETs, with cohesin enrichment and convergent CTCF orientation, only the PET with the highest confidence score was chosen.

No new targets for H9 hESC were designed, due to the assumption of TAD border conservation across cell types (Krefting et al. 2018). To validate this assumption, embryonic stem cell and K562 interaction frequencies were compared in Juicebox (Robinson et al. 2018) using publicly available data from HiC experiments of H1 hESC (Dekker et al. 2017) and K562 (Rao et al. 2014). H1 hESC HiC data was used as a proxy for H9 hESC. Both HiC maps had high read depths (>1x$10^9$ reads) and used the same restriction enzyme. A HiC score, defined as the $\log_{10}$of the observed/expected ratio (Engreitz et al. 2012), was then used to compare H1 hESC and K562 interaction. Narrower bins were used for the proximity groups (5 kb) compared to the non-proximity groups (25-50 kb) to obtain enough observations for a ratio (Supplemental Fig S13).

**sgRNA design**

All sgRNAs with predicted high efficiencies based on the Doench 2016 score (Doench et al. 2016) were designed using the CRISPOR online tool (Concordet and Haeussler 2018). FAIRE-seq data from ENCODE (ENCSR000DCM) (Davis et al. 2018) were used to ensure targeting of loci with similar chromatin accessibility for Cas9 (Jensen et al. 2017). The binding of Cas9 to DNA is directed by the position of the PAM

on either the Watson (W) or the Crick (C) strand. Directing one sgRNA in an sgRNA pair to the W strand and the other sgRNA to the C strand (W/C orientation) has been shown to reduce potentially confounding +1 templated insertions (Guo et al. 2018). The sgRNA pairs AB, CD and EF were therefore designed in this orientation. However, this was not possible for the sgRNA pairs GX due to the reuse of the A or B sgRNAs.

sgRNAs were purchased from Synthego (USA), and purified Cas9-nuclease from IDT. The sequences, orientation, MIT specificity scores and predicted efficiencies are provided in Supplemental Table S2. All sgRNA efficiencies were evaluated by indel frequencies using the Inference of CRISPR Edits (ICE) tool from Synthego (Conant et al. 2022) in both K562 cells (Supplemental Table S7) and H9 hESC (Supplemental Table 8). For this experiment, amplicons were obtained from both edited and non-edited DNA extracted 48 to 72 hours post electroporation (see primer sequences in Supplemental Table S5). To purify amplicons, ThermoFisher Scientific (USA) GeneJET Gel Extraction or PCR Purification Kit were used. Sanger sequencing was performed by Eurofins Genomics (Germany). Individual sgRNA efficiencies were then evaluated for differences between groups and their correlation with SV frequency was assessed.

**Electroporation of Cas9 RNPs**

An electroporation protocol was used to transfect cells with individual sgRNA pairs (Laustsen and Bak 2019). To assemble RNPs with the sgRNA pairs, 6 µg Cas9 enzyme (0.6 µL of 10 µg/µL) was mixed with 1.6 µg (0.5 µL of 3.2 µg/µL) of each of the two sgRNAs in PCR tubes in no predefined order. RNPs were then stored at -20℃ or used immediately. Before electroporation, K562 cells were grown in RPMI (+ L-glutamine) with 10% fetal bovine serum (FBS) and 100 U/µg per mL of penicillin/streptomycin (P/S) in T25 flasks and passaged when confluent. H9 hESC were grown on vitronectin XF in TeSR-E8 with 50 U/µg per mL of P/S, passaged weekly using PBS--/EDTA (0.5 mM) buffer and supplemented with TeSR-E8 with 10 µM ROCKi for 24 hours after each passage. The morphology of the hESC colonies was evaluated by phase-contrast microscopy during maintenance. Expression of pluripotency markers OCT4/POU5F1 and TRA-1-60 was confirmed by immunocytochemistry (Supplemental Fig S7).

For nucleofection of K562 cells, 20 µL of cells in OptiMem (37,500 cells/ µL) with RNPs were electroporated using program CM138 on the Lonza 4D-Nucleofector, then incubated in T25 flasks with RPMI complete medium (+FBS + P/S) at 200,000 cells/mL. The sgRNA pairs were electroporated individually but simultaneously for all six different chromosomes except the sgRNA pairs GX targeting non-related TAD borders, as it was not part of the original design, and the sgRNA pair EF for Chr10 (see Experimental design). For nucleofection of H9 hESC, areas of differentiation were aspirated before single-cell dissociation

of the colonies with accutase. 20 uL of cells were resuspended in P3 complete buffer (15,000 cells/µL), electroporated with RNPs using program CB-150 and split into two separate cultures wells with E8 medium supplemented with 10 µM ROCKi.

**DNA extraction**

Genomic DNA from approximately 200,000 cells was extracted at 3, 6, 12, 24, and 72 hours after electroporation to assess SV formation over time using ThermoFisher's Purelink Genomic Mini DNA kit. DNA was quantified on NanoDrop, normalized to 25 ng/uL, and stored at -20°C.

**Quantification of SV events**

A gain-of-signal ddPCR protocol was used to quantify SV formation (Watry et al. 2020). HEX reference probes were ordered from BioRad, FAM probes from IDT with 5'6-FAM/ZEN/3'IBFQ modifications (Supplemental Table S4). Primers were designed using Primer3Plus with the settings recommended for ddPCR by BioRad Laboratories Inc (USA). Amplicon and primer specificities were evaluated with the NCBI BLAST tool (Ye et al. 2012), and Mfold was used to verify the absence of strong secondary structures at the primer binding sites (Zuker 2003). Additionally, the primer target sequences were analyzed for SNPs in K562 cells (Zhou et al. 2019). All ddPCR primer pairs were validated beforehand with regular PCR using ddPCR settings and enzyme (primer sequences in Supplemental Table S3).

To avoid inaccurate DNA normalization due to K562 cells' aneuploidy (Zhou et al. 2019), different reference HEX assays were placed in physical proximity of the FAM probe for each chromosome. This normalization approach was validated with ddPCR before proceeding to quantification of SVs (see Supplemental Fig S8).

**ddPCR protocol**

For each assay, sterile PCR tubes with 1.68 µL of 25 ng/µL DNA (40 ng + 5%) from each extraction point were prepared in addition to a negative control and a no template control with ddH2O. Then, 19.32 µL of the master mix containing all other components was added to each PCR tube, yielding a final volume of 21 µL of ddPCR mixture. Droplets containing 20 µL of ddPCR mixture were generated, transferred to a 96-well ddPCR plate, and heat-sealed. Samples were run in a Bio-Rad C1000 Thermal Cycler at ramp rate 2℃/s for the following steps: 1) 95℃ for 10 min, 2) 94℃ for 30s, 3) 60℃ for 1 min, 4) 98℃ for 10 min (step 2-3 x40). The QX200 Droplet Reader was used to analyze droplets, QX manager 1.2 was used to process results. The negative control was used to gate the FAM channel (the SV detecting probe), and the no-template-control (NTC) to gate the HEX channel (the reference).

**Validation of ddPCR quantification with single cell clones**

One sample was randomly selected for single cell cloning. After the 72h extraction, leftover cells were sorted into a 96-well V plate with 100 µl of RPMI complete medium using the BD FACSAria III and transferred to a 96-well U plate after 2-3 weeks. Once colonies reached confluency, DNA was extracted using Quickextract from Lucigen. PCR was conducted to detect deletions by band separation using the Phusion Polymerase from ThermoFisher Scientific (Mullis et al. 1986). The following conditions were used for PCR: 1) 98℃ for 30s, 2) 98℃ for 10s, 3) x℃ for 30s, 4) 72℃ for 25s, 5) 72℃ for 10 min (step 2-4 repeated x35). X was approximated using the Tm calculator from ThermoFisher. Results can be seen in Supplemental Fig S9.

**High-throughput sequencing**

Twenty chimeric deletion-junctions (five from each of the AB, CD, EF and GX sgRNA pairs) were successfully sequenced using Eurofin Genomics´ NGSelect service on the Illumina MiSeq platform. Primer sequences can be found in Supplemental Table S6. FASTQ files were analyzed using the Cas-Analyzer online tool (Park et al. 2017) with the following parameters: R: 113, n: 0, r: 5. R=113 would set the analysis range using linker sequences of 13 bp, allowing 100 bp up- and downstream of the ligation site to be analyzed for resection and insertion events, n=0 would set the minimum frequency for an event, whereas r=5 would define a wild-type sequence of 10 bp around the ligation site that would mark a read as perfect repair if present . These parameters were used to homogenize readouts across differences in amplicon lengths. Adjusting the position of the linker sequences allowed us to quantify ddPCR sensitivity (Supplemental Fig S10).

All chimeric deletion junctions were assessed for precise ligation and microhomology-usage using an R script from Beying et al. (Beying et al. 2020). Precise ligation was defined as the proportion of reads with no resections or insertions at the predicted ligation site, normalized to the total number of reads. Reads with 1-2 bp insertions were included in this precise ligation definition to account for templated insertions (Guo et al. 2018), and so were reads with 1-2 bp resections to account for Cas9-generated staggered ends (Xue and Greene 2021). The R script analyzed microhomology-usage by comparing sequences before and after a resection for homology. A read was classified as using microhomology if one or more matching bases were found at the resection junction. Reads identified as using microhomology for ligation were then normalized to the subset of reads with resection.

### Statistical analysis

The results were reported as group medians with error bars showing the interquartile range due to the non-normal distribution of the data. Statistical comparisons were made with non-parametric tests. Comparisons between groups were made with the two-sided Mann-Whitney *U* test. Comparisons within the same samples were made with the two-sided Wilcoxon matched-pairs signed rank test. Correlation was assessed using Spearman's rank correlation coefficient. Statistical significance was considered at a significance level of 0.05. Statistical tests were performed in GraphPad Prism.

## Data access

The high-throughput sequencing data generated in this study have been submitted to the NCBI BioProject database (https://www.ncbi.nlm.nih.gov/bioproject/) under accession number PRJNA1117804.

## Competing interest statement

R.O.B is a co-founder of and consultant to UNIKUM Tx and is co-inventor on patents and patent applications related to gene editing. UNIKUM Tx was not involved in the present study.

## Acknowledgements

Thanks to Holger Puchta's lab at Karlsruhe Institute of Technology for help with analyzing high-throughput sequencing data. Thanks to Mark Denham's lab at Aarhus University for H9 hESC cells. This work was funded (UBJ) by the Independent Research Fund Denmark GRANT# 1149-00024B and 9039-00337B. Conceptualization: UBJ; methodology: MDJ, TT, ROB; formal analysis: MDJ, TT, ROB, UBJ; investigation: MDJ, TT, ROB, UBJ; resources: ROB, UBJ; writing - original draft: MDJ, UBJ, TT; writing - review & editing: MDJ, TT, ROB, UBJ; visualization: MDJ, TT, UBJ; supervision: TT, ROB, UBJ; funding acquisition: UBJ, ROB. All authors read and approved the final manuscript.

## References

Akdemir KC, Le VT, Chandran S, Li Y, Verhaak RG, Beroukhim R, Campbell PJ, Chin L, Dixon JR, Futreal PA. 2020. Disruption of chromatin folding domains by somatic genomic rearrangements in human cancer. *Nature genetics* **52**: 294-305.

Arnould C, Rocher V, Saur F, Bader AS, Muzzopappa F, Collins S, Lesage E, Le Bozec B, Puget N, Clouaire T et al. 2023. Chromatin compartmentalization regulates the response to DNA damage. *Nature* **623**: 183-192.

Aten JA, Stap J, Krawczyk PM, van Oven CH, Hoebe RA, Essers J, Kanaar R. 2004. Dynamics of DNA double-strand breaks revealed by clustering of damaged chromosome domains. *Science* **303**: 92-95.

Aymard F, Aguirrebengoa M, Guillou E, Javierre BM, Bugler B, Arnould C, Rocher V, Iacovoni JS, Biernacka A, Skrzypczak M et al. 2017. Genome-wide mapping of long-range contacts unveils clustering of DNA double-strand breaks at damaged active genes. *Nat Struct Mol Biol* **24**: 353-361.

Balajee AS, Sanders JT, Golloshi R, Shuryak I, McCord RP, Dainiak N. 2018. Investigation of Spatial Organization of Chromosome Territories in Chromosome Exchange Aberrations After Ionizing Radiation Exposure. *Health Phys* **115**: 77-89.

Beagan JA, Phillips-Cremins JE. 2020. On the existence and functionality of topologically associating domains. *Nat Genet* **52**: 8-16.

Bergman S, Tuller T. 2024. Strong association between genomic 3D structure and CRISPR cleavage efficiency. *PLoS Comput Biol* **20**: e1012214.

Beying N, Schmidt C, Pacher M, Houben A, Puchta H. 2020. CRISPR-Cas9-mediated induction of heritable chromosomal translocations in Arabidopsis. *Nat Plants* **6**: 638-645.

Biehs R, Steinlage M, Barton O, Juhász S, Künzel J, Spies J, Shibata A, Jeggo PA, Löbrich M. 2017. DNA Double-Strand Break Resection Occurs during Non-homologous End Joining in G1 but Is Distinct from Resection during Homologous Recombination. *Mol Cell* **65**: 671-684.e675.

Canela A, Maman Y, Jung S, Wong N, Callen E, Day A, Kieffer-Kwon KR, Pekowska A, Zhang H, Rao SSP et al. 2017a. Genome Organization Drives Chromosome Fragility. *Cell* **170**: 507-521.e518.

Canela A, Maman Y, Jung S, Wong N, Callen E, Day A, Kieffer-Kwon KR, Pekowska A, Zhang H, Rao SSP et al. 2017b. Genome Organization Drives Chromosome Fragility. *Cell* **170**: 507-521 e518.

Canoy RJ, Shmakova A, Karpukhina A, Shepelev M, Germini D, Vassetzky Y. 2022. Factors That Affect the Formation of Chromosomal Translocations in Cells. *Cancers (Basel)* **14**.

Chang HHY, Pannunzio NR, Adachi N, Lieber MR. 2017. Non-homologous DNA end joining and alternative pathways to double-strand break repair. *Nat Rev Mol Cell Biol* **18**: 495-506.

Chang LH, Ghosh S, Noordermeer D. 2020. TADs and Their Borders: Free Movement or Building a Wall? *J Mol Biol* **432**: 643-652.

Choi PS, Meyerson M. 2014. Targeted genomic rearrangements using CRISPR/Cas technology. *Nat Commun* **5**: 3728.

Conant D, Hsiau T, Rossi N, Oki J, Maures T, Waite K, Yang J, Joshi S, Kelso R, Holden K et al. 2022. Inference of CRISPR Edits from Sanger Trace Data. *CRISPR J* **5**: 123-130.

Concordet JP, Haeussler M. 2018. CRISPOR: intuitive guide selection for CRISPR/Cas9 genome editing experiments and screens. *Nucleic Acids Res* **46**: W242-W245.

Cullot G, Boutin J, Toutain J, Prat F, Pennamen P, Rooryck C, Teichmann M, Rousseau E, Lamrissi-Garcia I, Guyonnet-Duperat V et al. 2019. CRISPR-Cas9 genome editing induces megabase-scale chromosomal truncations. *Nat Commun* **10**: 1136.

Davis CA, Hitz BC, Sloan CA, Chan ET, Davidson JM, Gabdank I, Hilton JA, Jain K, Baymuradov UK, Narayanan AK et al. 2018. The Encyclopedia of DNA elements (ENCODE): data portal update. *Nucleic Acids Res* **46**: D794-D801.

Dekker J, Belmont AS, Guttman M, Leshyk VO, Lis JT, Lomvardas S, Mirny LA, O'Shea CC, Park PJ, Ren B et al. 2017. The 4D nucleome project. *Nature* **549**: 219-226.

DiBiase SJ, Zeng ZC, Chen R, Hyslop T, Curran WJ, Jr., Iliakis G. 2000. DNA-dependent protein kinase stimulates an independently active, nonhomologous, end-joining apparatus. *Cancer Res* **60**: 1245-1253.

Dixon JR, Selvaraj S, Yue F, Kim A, Li Y, Shen Y, Hu M, Liu JS, Ren B. 2012. Topological domains in mammalian genomes identified by analysis of chromatin interactions. *Nature* **485**: 376-380.

Doench JG, Fusi N, Sullender M, Hegde M, Vaimberg EW, Donovan KF, Smith I, Tothova Z, Wilen C, Orchard R et al. 2016. Optimized sgRNA design to maximize activity and minimize off-target effects of CRISPR-Cas9. *Nature biotechnology* **34**: 184-191.

Eidelman Y, Salnikov I, Slanina S, Andreev S. 2021. Chromosome Folding Promotes Intrachromosomal Aberrations under Radiation- and Nuclease-Induced DNA Breakage. *Int J Mol Sci* **22**.

Engreitz JM, Agarwala V, Mirny LA. 2012. Three-dimensional genome architecture influences partner selection for chromosomal translocations in human disease. *PloS one* **7**: e44196.

Eres IE, Gilad Y. 2021. A TAD Skeptic: Is 3D Genome Topology Conserved? *Trends in genetics : TIG* **37**: 216-223.

Frit P, Ropars V, Modesti M, Charbonnier JB, Calsou P. 2019. Plugged into the Ku-DNA hub: The NHEJ network. *Prog Biophys Mol Biol* **147**: 62-76.

Fudenberg G, Imakaev M, Lu C, Goloborodko A, Abdennur N, Mirny LA. 2016. Formation of Chromosomal Domains by Loop Extrusion. *Cell Rep* **15**: 2038-2049.

Gandhi M, Medvedovic M, Stringer JR, Nikiforov YE. 2006. Interphase chromosome folding determines spatial proximity of genes participating in carcinogenic RET/PTC rearrangements. *Oncogene* **25**: 2360-2366.

Ghezraoui H, Piganeau M, Renouf B, Renaud JB, Sallmyr A, Ruis B, Oh S, Tomkinson AE, Hendrickson EA, Giovannangeli C et al. 2014. Chromosomal translocations in human cells are generated by canonical nonhomologous end-joining. *Mol Cell* **55**: 829-842.

Gu W, Zhang F, Lupski JR. 2008. Mechanisms for human genomic rearrangements. *Pathogenetics* **1**: 4.

Guo T, Feng YL, Xiao JJ, Liu Q, Sun XN, Xiang JF, Kong N, Liu SC, Chen GQ, Wang Y et al. 2018. Harnessing accurate non-homologous end joining for efficient precise deletion in CRISPR/Cas9-mediated genome editing. *Genome Biol* **19**: 170.

Höijer I, Emmanouilidou A, Östlund R, van Schendel R, Bozorgpana S, Tijsterman M, Feuk L, Gyllensten U, den Hoed M, Ameur A. 2022. CRISPR-Cas9 induces large structural variants at on-target and off-target sites in vivo that segregate across generations. *Nat Commun* **13**: 627.

Jensen KT, Floe L, Petersen TS, Huang J, Xu F, Bolund L, Luo Y, Lin L. 2017. Chromatin accessibility and guide sequence secondary structure affect CRISPR-Cas9 gene editing efficiency. *FEBS Lett* **591**: 1892-1901.

Krefting J, Andrade-Navarro MA, Ibn-Salem J. 2018. Evolutionary stability of topologically associating domains is associated with conserved gene regulation. *BMC Biol* **16**: 87.

Laustsen A, Bak RO. 2019. Electroporation-Based CRISPR/Cas9 Gene Editing Using Cas9 Protein and Chemically Modified sgRNAs. *Methods in molecular biology (Clifton, NJ)* **1961**: 127-134.

Lee KJ, Saha J, Sun J, Fattah KR, Wang SC, Jakob B, Chi L, Wang SY, Taucher-Scholz G, Davis AJ et al. 2016. Phosphorylation of Ku dictates DNA double-strand break (DSB) repair pathway choice in S phase. *Nucleic Acids Res* **44**: 1732-1745.

Lieberman-Aiden E, van Berkum NL, Williams L, Imakaev M, Ragoczy T, Telling A, Amit I, Lajoie BR, Sabo PJ, Dorschner MO et al. 2009. Comprehensive mapping of long-range interactions reveals folding principles of the human genome. *Science (New York, NY)* **326**: 289-293.

Liu P, Carvalho CM, Hastings PJ, Lupski JR. 2012. Mechanisms for recurrent and complex human genomic rearrangements. *Curr Opin Genet Dev* **22**: 211-220.

Min YL, Bassel-Duby R, Olson EN. 2019. CRISPR Correction of Duchenne Muscular Dystrophy. *Annu Rev Med* **70**: 239-255.

Misteli T, Soutoglou E. 2009. The emerging role of nuclear architecture in DNA repair and genome maintenance. *Nat Rev Mol Cell Biol* **10**: 243-254.

Miyata M, Yoshida J, Takagishi I, Horie K. 2023. Comparison of CRISPR-Cas9-mediated megabase-scale genome deletion methods in mouse embryonic stem cells. *DNA Res* **30**.

Mullis K, Faloona F, Scharf S, Saiki R, Horn G, Erlich H. 1986. Specific enzymatic amplification of DNA in vitro: the polymerase chain reaction. *Cold Spring Harb Symp Quant Biol* **51 Pt 1**: 263-273.

Nikiforova MN, Stringer JR, Blough R, Medvedovic M, Fagin JA, Nikiforov YE. 2000. Proximity of chromosomal loci that participate in radiation-induced rearrangements in human cells. *Science* **290**: 138-141.

Park J, Lim K, Kim JS, Bae S. 2017. Cas-analyzer: an online tool for assessing genome editing results using NGS data. *Bioinformatics* **33**: 286-288.

Racko D, Benedetti F, Dorier J, Stasiak A. 2018. Transcription-induced supercoiling as the driving force of chromatin loop extrusion during formation of TADs in interphase chromosomes. *Nucleic Acids Res* **46**: 1648-1660.

Rao SS, Huntley MH, Durand NC, Stamenova EK, Bochkov ID, Robinson JT, Sanborn AL, Machol I, Omer AD, Lander ES et al. 2014. A 3D map of the human genome at kilobase resolution reveals principles of chromatin looping. *Cell* **159**: 1665-1680.

Riballo E, Kühne M, Rief N, Doherty A, Smith GC, Recio MJ, Reis C, Dahm K, Fricke A, Krempler A et al. 2004. A pathway of double-strand break rejoining dependent upon ATM, Artemis, and proteins locating to gamma-H2AX foci. *Mol Cell* **16**: 715-724.

Robinson JT, Turner D, Durand NC, Thorvaldsdóttir H, Mesirov JP, Aiden EL. 2018. Juicebox.js Provides a Cloud-Based Visualization System for Hi-C Data. *Cell Syst* **6**: 256-258.e251.

Rothkamm K, Kühne M, Jeggo PA, Löbrich M. 2001. Radiation-induced genomic rearrangements formed by nonhomologous end-joining of DNA double-strand breaks. *Cancer Res* **61**: 3886-3893.

Roukos V, Voss TC, Schmidt CK, Lee S, Wangsa D, Misteli T. 2013. Spatial dynamics of chromosome translocations in living cells. *Science* **341**: 660-664.

Sadowski M, Kraft A, Szalaj P, Wlasnowolski M, Tang Z, Ruan Y, Plewczynski D. 2019. Spatial chromatin architecture alteration by structural variations in human genomes at the population scale. *Genome Biol* **20**: 148.

Schmitt AD, Hu M, Jung I, Xu Z, Qiu Y, Tan CL, Li Y, Lin S, Lin Y, Barr CL et al. 2016. A Compendium of Chromatin Contact Maps Reveals Spatially Active Regions in the Human Genome. *Cell Rep* **17**: 2042-2059.

Selvaraj S, Feist WN, Viel S, Vaidyanathan S, Dudek AM, Gastou M, Rockwood SJ, Ekman FK, Oseghale AR, Xu L et al. 2024. High-efficiency transgene integration by homology-directed repair in human primary cells using DNA-PKcs inhibition. *Nature biotechnology* **42**: 731-744.

Sidiropoulos N, Mardin BR, Rodríguez-González FG, Bochkov ID, Garg S, Stütz AM, Korbel JO, Aiden EL, Weischenfeldt J. 2022. Somatic structural variant formation is guided by and influences genome architecture. *Genome research* **32**: 643-655.

Swenson KM, Blanchette M. 2019. Large-scale mammalian genome rearrangements coincide with chromatin interactions. *Bioinformatics* **35**: i117-i126.

Tang Z, Luo OJ, Li X, Zheng M, Zhu JJ, Szalaj P, Trzaskoma P, Magalska A, Wlodarczyk J, Ruszczycki B et al. 2015. CTCF-Mediated Human 3D Genome Architecture Reveals Chromatin Topology for Transcription. *Cell* **163**: 1611-1627.

Uematsu N, Weterings E, Yano K, Morotomi-Yano K, Jakob B, Taucher-Scholz G, Mari PO, van Gent DC, Chen BP, Chen DJ. 2007. Autophosphorylation of DNA-PKCS regulates its dynamics at DNA double-strand breaks. *J Cell Biol* **177**: 219-229.

Watanabe G, Lieber MR. 2023. The flexible and iterative steps within the NHEJ pathway. *Prog Biophys Mol Biol* **180-181**: 105-119.

Watry HL, Feliciano CM, Gjoni K, Takahashi G, Miyaoka Y, Conklin BR, Judge LM. 2020. Rapid, precise quantification of large DNA excisions and inversions by ddPCR. *Scientific reports* **10**: 14896.

Wu J, Zou Z, Liu Y, Liu X, Zhangding Z, Xu M, Hu J. 2022. CRISPR/Cas9-induced structural variations expand in T lymphocytes in vivo. *Nucleic Acids Res* **50**: 11128-11137.

Wu P, Li T, Li R, Jia L, Zhu P, Liu Y, Chen Q, Tang D, Yu Y, Li C. 2017. 3D genome of multiple myeloma reveals spatial genome disorganization associated with copy number variations. *Nat Commun* **8**: 1937.

Xue C, Greene EC. 2021. DNA Repair Pathway Choices in CRISPR-Cas9-Mediated Genome Editing. *Trends in genetics : TIG* **37**: 639-656.

Ye J, Coulouris G, Zaretskaya I, Cutcutache I, Rozen S, Madden TL. 2012. Primer-BLAST: a tool to design target-specific primers for polymerase chain reaction. *BMC Bioinformatics* **13**: 134.

Yoshioka KI, Kusumoto-Matsuo R, Matsuno Y, Ishiai M. 2021. Genomic Instability and Cancer Risk Associated with Erroneous DNA Repair. *Int J Mol Sci* **22**.

Zhang Y, McCord RP, Ho YJ, Lajoie BR, Hildebrand DG, Simon AC, Becker MS, Alt FW, Dekker J. 2012. Spatial organization of the mouse genome and its role in recurrent chromosomal translocations. *Cell* **148**: 908-921.

Zhou B, Ho SS, Greer SU, Zhu X, Bell JM, Arthur JG, Spies N, Zhang X, Byeon S, Pattni R et al. 2019. Comprehensive, integrated, and phased whole-genome analysis of the primary ENCODE cell line K562. *Genome research* **29**: 472-484.

Zuker M. 2003. Mfold web server for nucleic acid folding and hybridization prediction. *Nucleic Acids Res* **31**: 3406-3415.

# Figure legends

**Fig 1.** The effect of spatial proximity on SV frequency was measured in K562 cells. **(A)** Six TADs were identified in K562 cells and named according to their position: Chr2, Chr6, Chr10, Chr17, Chr21 and ChrX. Seven sgRNAs were designed for each TAD to investigate spatial proximity effects: sgRNAs A and B, which targeted sequences inside the CTCF motif at the left and right TAD border; sgRNAs C and D, which targeted sequences outside the CTCF motif at the left and right TAD border; sgRNA E, which targeted an intra-TAD sequence; sgRNA F, which targeted a sequence outside the TAD, and sgRNA G, which targeted a sequence inside the CTCF motif of a neighboring TAD. Individual sgRNAs were electroporated into K562 cells in separate pairs as AB, CD, EF and GX (X could be sgRNA A or B). All pairs would have the same distance in base pairs between them, but AB and CD would be in spatial proximity, whereas EF and GX would be spatially distant. **(B)** An example Hi-C map of the Chr6 TAD. **(C)** Illustration of the gain-of-signal ddPCR assay with primers surrounding the cut sites of the sgRNA pair and the binding site of the FAM probe. The HEX probe included to adjust for locus copy number is also illustrated. **(D)** SV frequencies (deletions + inversions) for AB, CD, EF and GX sgRNA pairs (n = 6 sgRNA pairs in each group; six chromosome loci with one sgRNA pair); p-values from Mann-Whitney *U* test. (**E)** SV frequencies between proximity and non-proximity sgRNA pairs (n = 12 sgRNA pairs in each group; six chromosome loci with two sgRNA pairs); p-value from Mann-Whitney *U* test. **(F)** Individual sgRNA efficiencies measured by their ability to induce indels (n = 24 sgRNAs in each group; six chromosome loci with four sgRNAs); p-value from Mann-Whitney *U* test. (**G)** Frequencies of deletions and inversions for all sgRNA pairs (n = 24 sgRNA pairs in each group; six chromosome loci with four sgRNA pairs); p-value from Wilcoxon matched-pairs signed rank test. The observations are biological replicates, and the error bars show the median and IQR.

**Fig 2.** The effect of spatial proximity on SV frequency was measured in H9 hESC at the Chr2, Chr6, Chr17, Chr21 and ChrX loci. **(A)** SV frequencies for AB, CD, EF and GX sgRNA pairs (n = 5 sgRNA pairs in each group; five chromosome loci with one sgRNA pair); p-values from Mann-Whitney *U* test. **(B)** SV frequencies between proximity and non-proximity sgRNA pairs (n = 10 sgRNA pairs in each group; five chromosome loci with two sgRNA pairs); p-value from Mann-Whitney *U* test. **(C)** Overall frequencies of deletions and inversions (n = 20 sgRNA pairs in each group; five chromosome loci with four sgRNA pairs); p-value from Wilcoxon matched-pairs signed rank test. (**D)** Individual sgRNA efficiencies by indel frequency (n = 20 sgRNAs in each group; five chromosome loci with four sgRNAs); p-value from Mann-Whitney *U* test. The observations are biological replicates, and the error bars show the median and IQR.

**Fig 3.** SV frequency was determined at 3, 6, 12 and 24 hours after electroporation in K562 cells and normalized to the end-point SV frequency for each sgRNA pair as a measure of SV formation speed. **(A)** Formation speed of deletions for sgRNA pairs AB, CD, EF and GX (n = 6 sgRNA pairs in each group; six chromosome loci with one sgRNA pair). **(B)** Formation speed of deletions for proximity vs. non-proximity sgRNA pairs. (n = 12 sgRNA pairs in each group; six chromosome loci with two sgRNA pairs); p-values from Mann-Whitney *U* test. **(C)** Formation speed of inversions for sgRNA pairs AB, CD, EF and GX (n = 6 sgRNA pairs in each group; six chromosome loci with one sgRNA pair). **(D)** Formation speed of inversions for proximity vs. non-proximity sgRNA pairs. (n = 12 sgRNA pairs in each group; six chromosome loci with two sgRNA pairs); p-values from Mann-Whitney *U* test. **(E)** Formation speed of deletions vs. inversions (n = 24 sgRNA pairs in each group; six chromosome loci with four sgRNA pairs); p-values from Wilcoxon matched-pairs signed rank test. The observations are biological replicates, and the error bars show the median and IQR.

**Fig 4.** Five chimeric deletion junctions produced from each of the sgRNA pairs AB, CD, EF and GX were analyzed with Illumina MiSeq Amplicon Sequencing. **(A)** Definition of a chimeric deletion junction. **(B)** Characterization of sequencing reads. **(C)** Read distributions for the proximity and non-proximity sgRNA pairs (n = 10 sgRNA pairs in each group; six chromosome loci with one to two sgRNA pairs). **(D)** Precise ligation of chimeric deletion junctions for proximity and non-proximity sgRNA pairs (n = 10 sgRNA pairs in each group; six chromosome loci with one to two sgRNA pairs); p-value from Mann-Whitney *U* test. **(E)** Microhomology usage normalized to all reads with resection for proximity and non-proximity sgRNA pairs (n = 10 sgRNA pairs in each group; six chromosome loci with one to two sgRNA pairs); p-value from Mann-Whitney *U* test. The observations are biological replicates, and the error bars show the median and IQR.

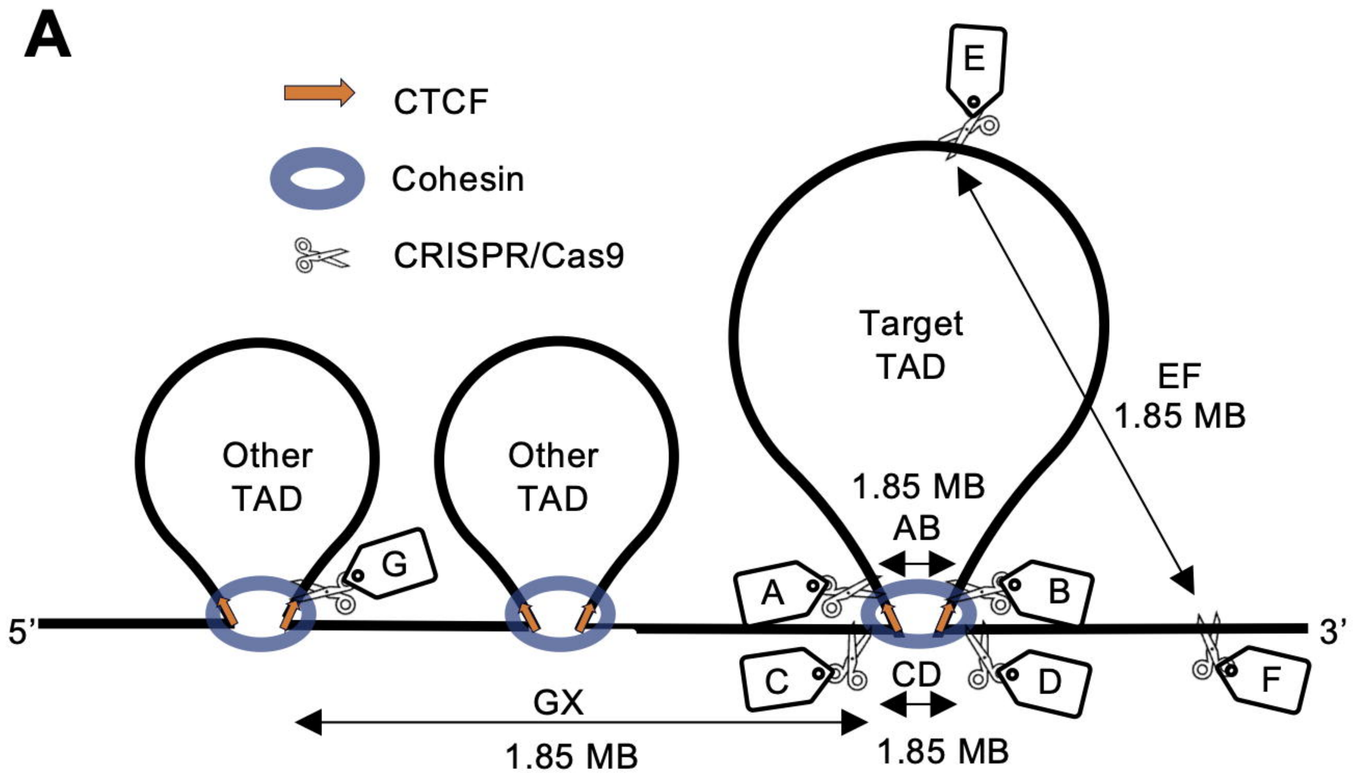


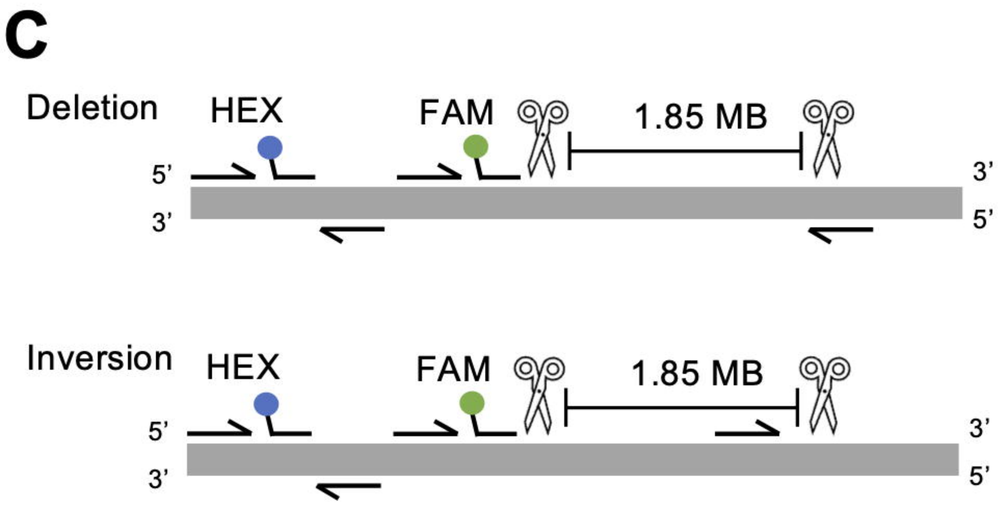


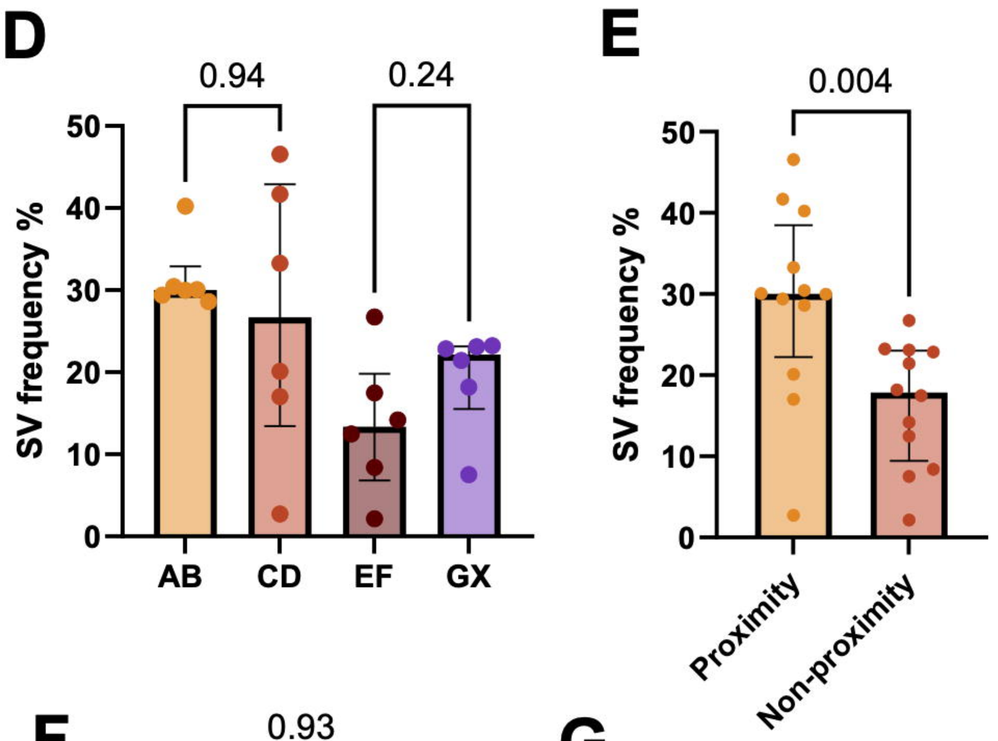


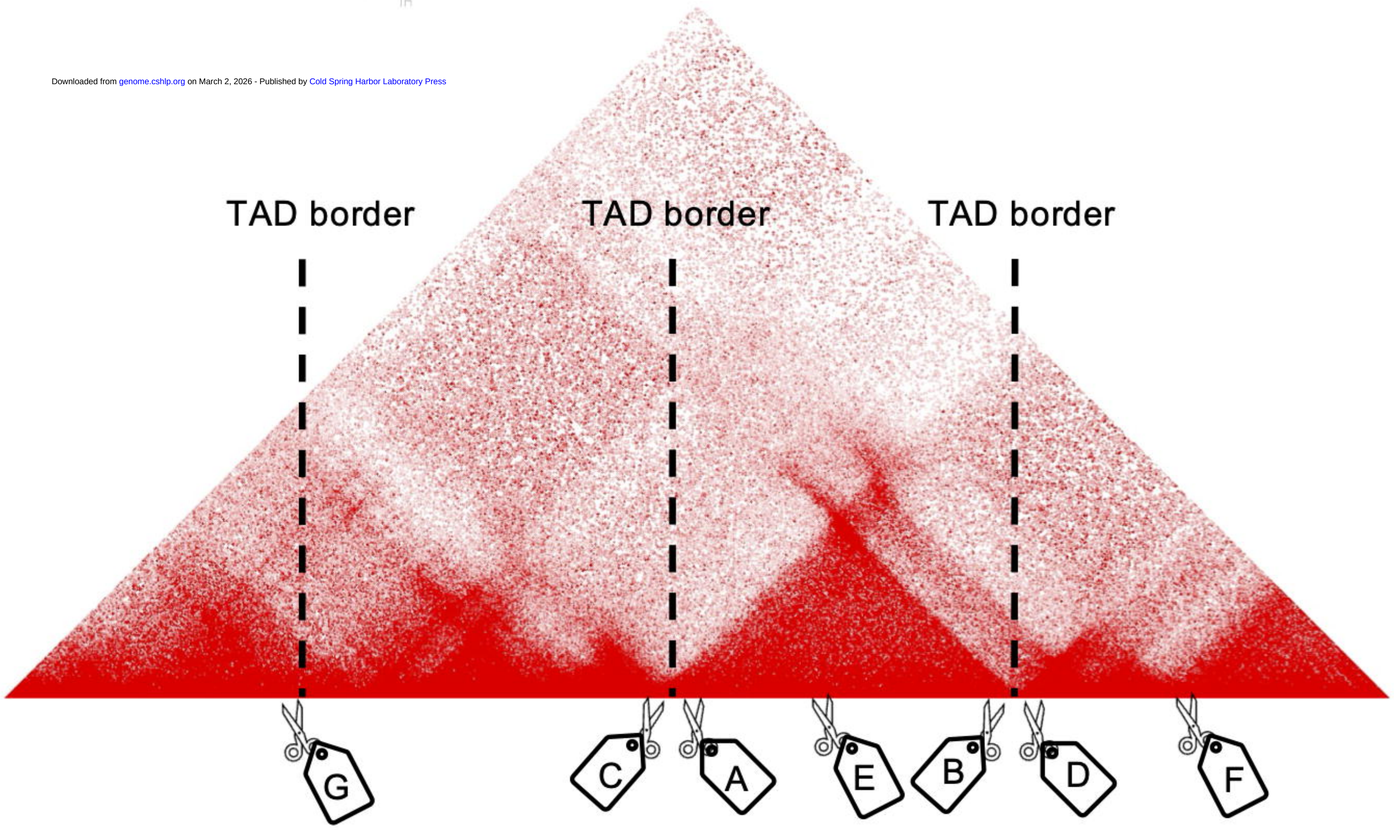




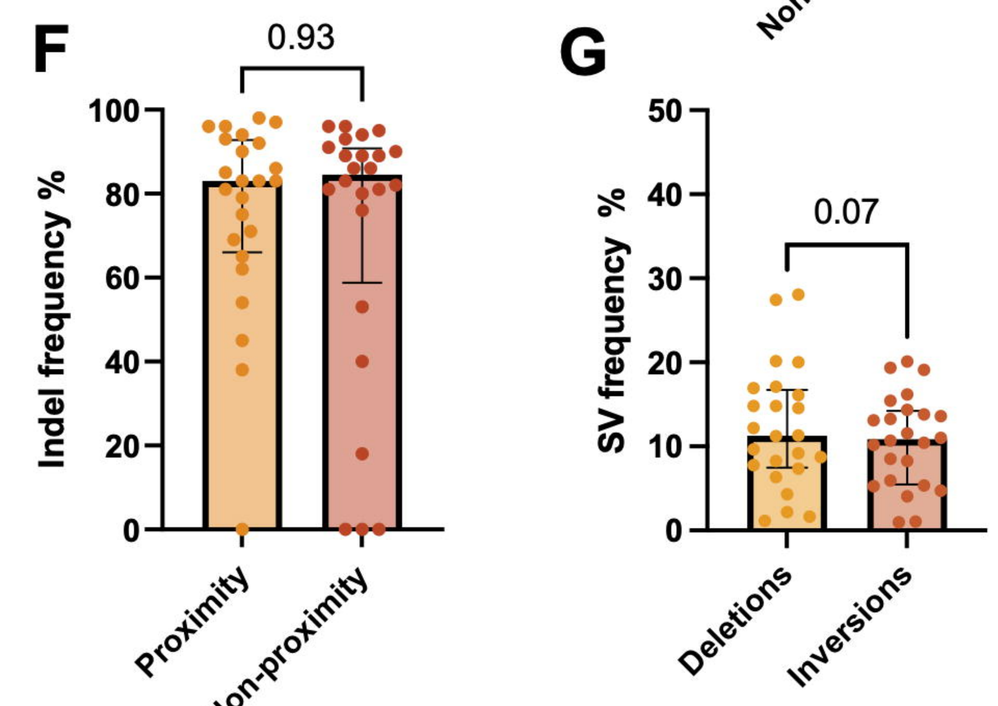

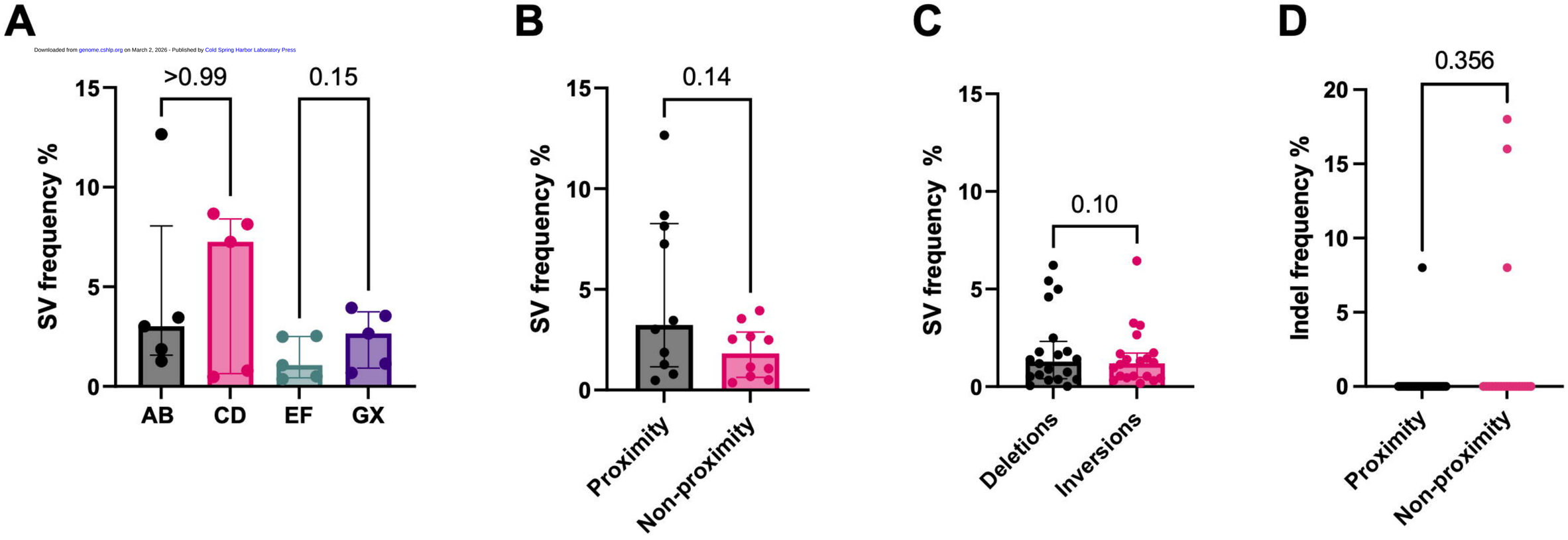

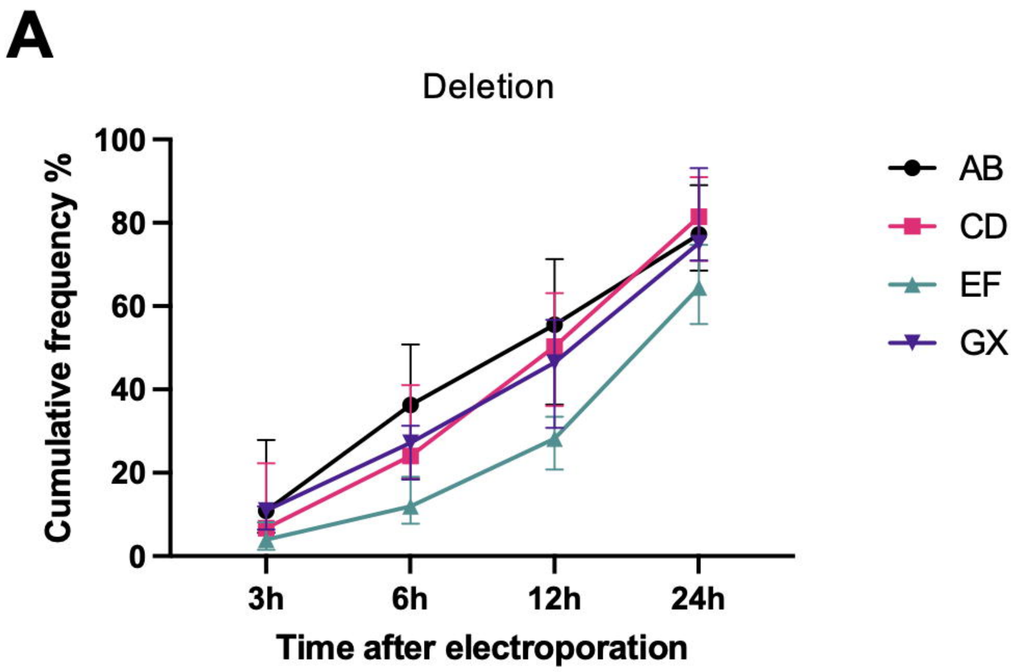


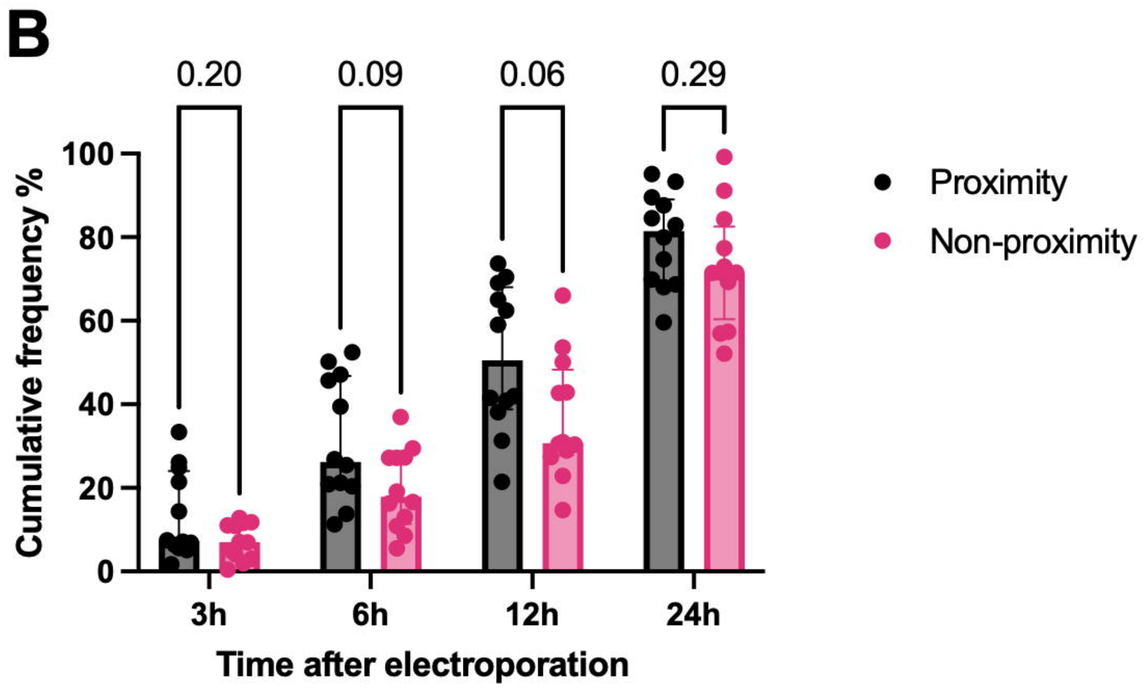


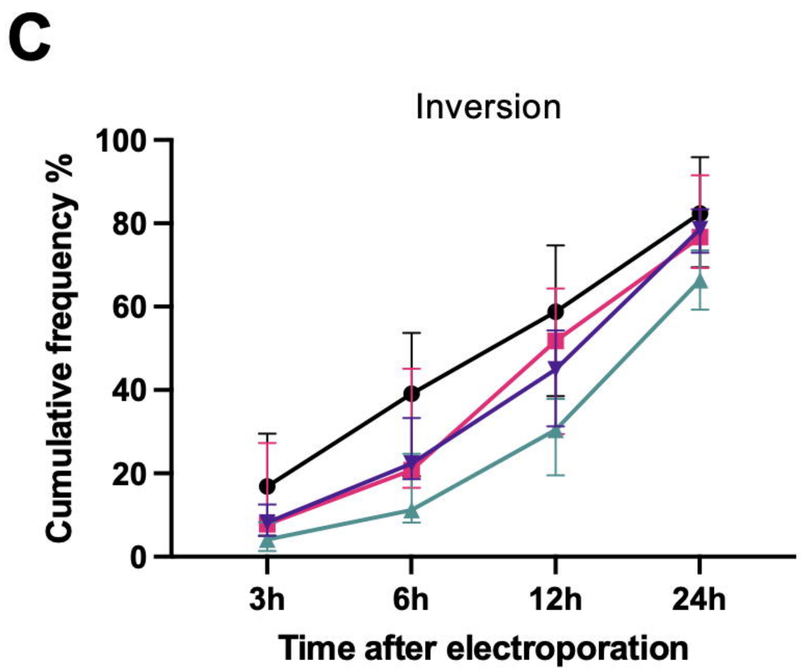


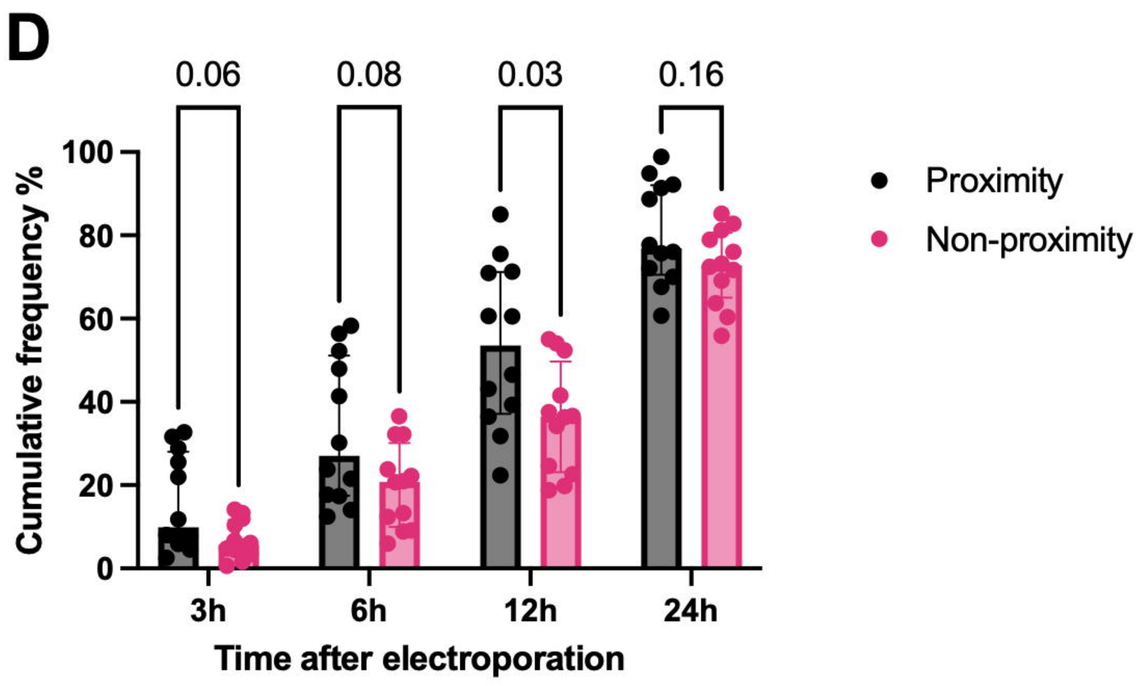




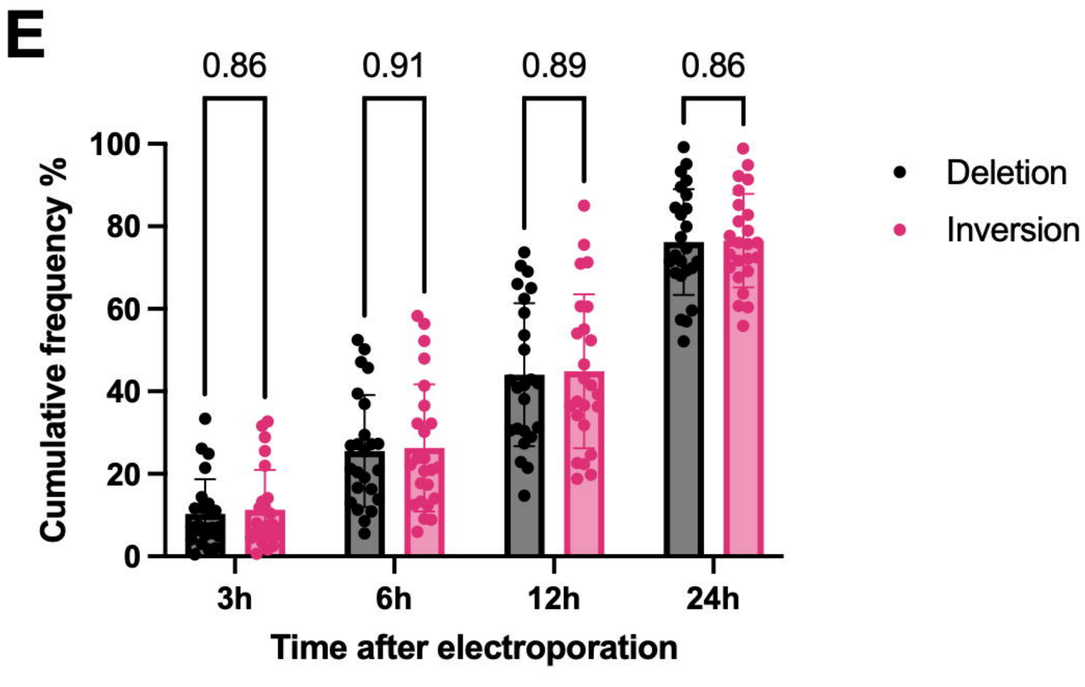

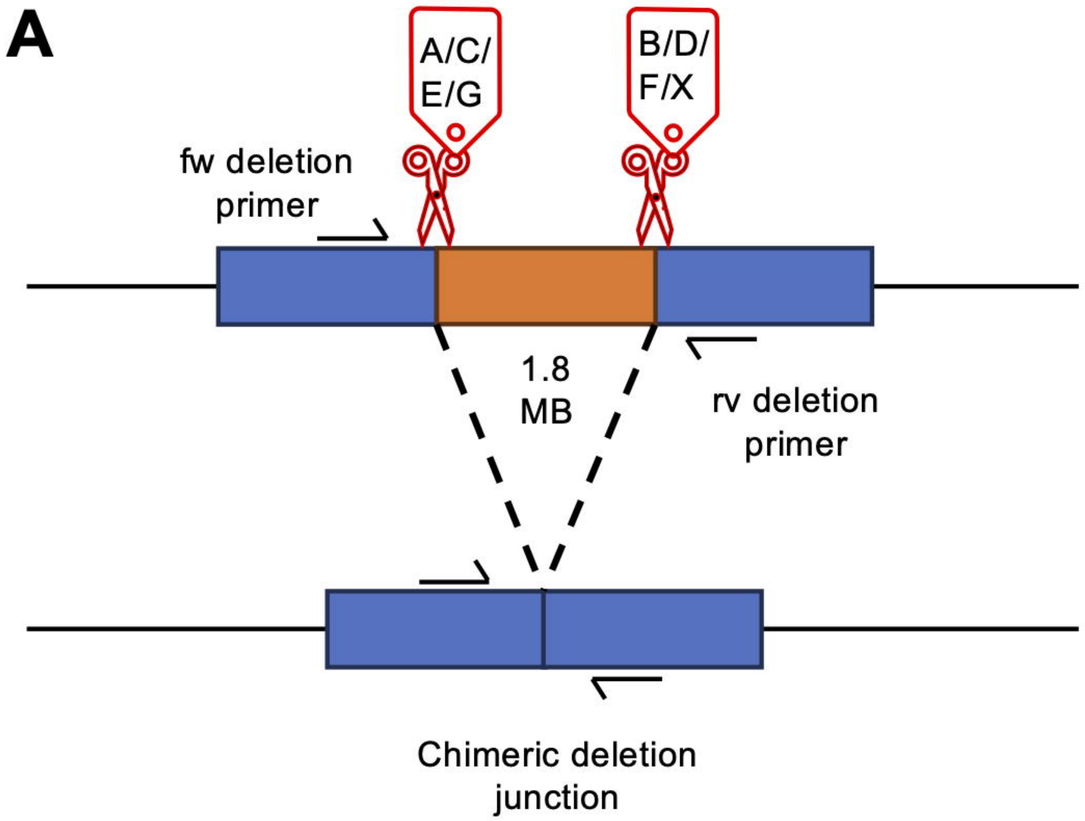


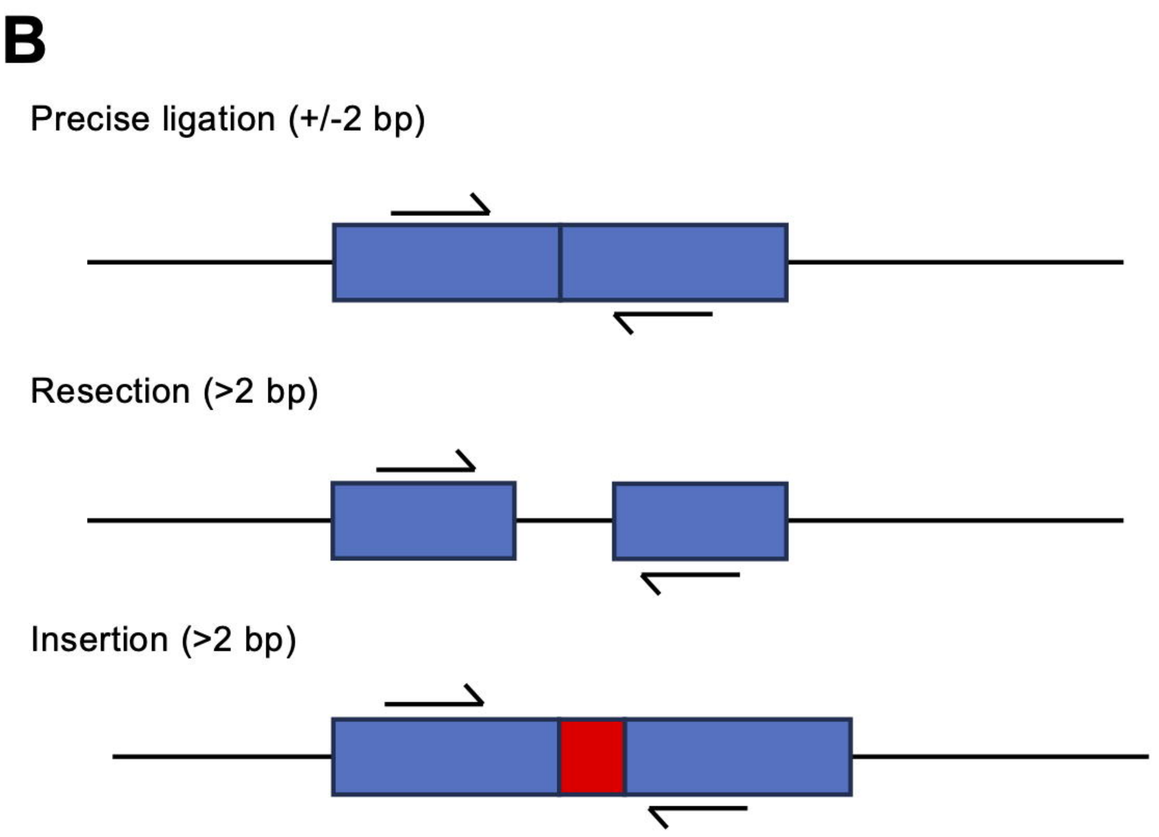


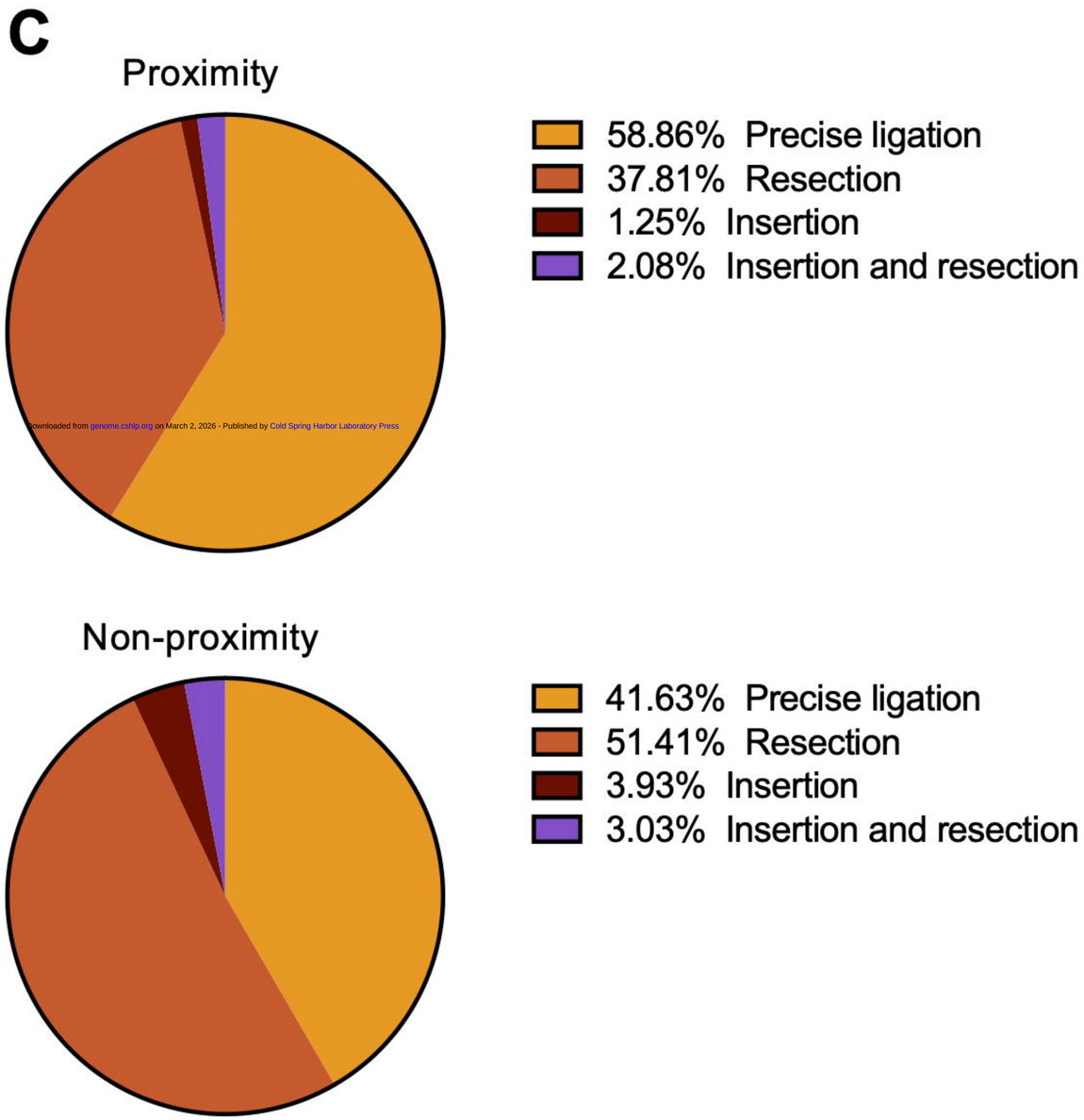




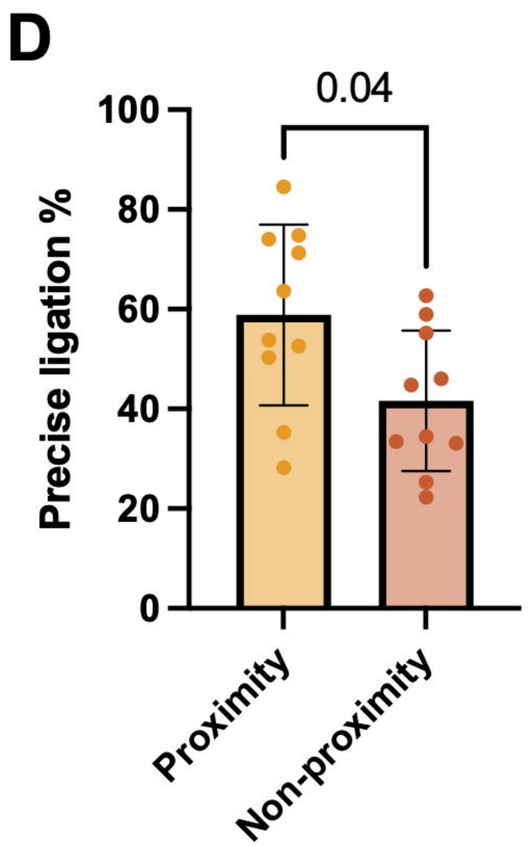


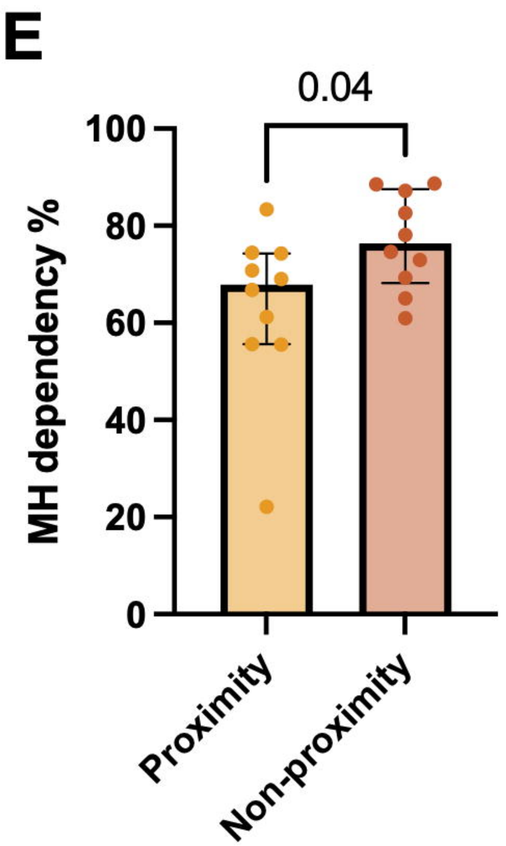

# Characterization of the role of spatial proximity of DNA double-strand breaks in the formation of CRISPR-Cas9-induced large structural variations

Mikkel Dahl-Jessen, Thorkild Terkelsen, Rasmus O Bak, et al.

*Genome Res.* published online January 13, 2025
Access the most recent version at doi:10.1101/gr.278575.123